https://ntrs.nasa.gov/search.jsp?R=20170003361 2019-08-29T23:33:45+00:00Z

Testing the Two-Layer Model for Correcting Near Cloud Reflectance Enhancement Using LES/SHDOM Simulated Radiances

GUOYONG WEN[1,2], ALEXANDER MARSHAK[1], TAMÁS VÁRNAI[1,3], AND ROBERT LEVY[1]

Short title: Near-cloud Reflectance for Aerosol Retrievals

(for submission to *Journal of Geophysical Research*)

[1]NASA Goddard Space Flight Center, Greenbelt, Maryland
[2]GESTAR/Morgan State University, Maryland
[3]University of Maryland Baltimore County, Baltimore, Maryland

Authors

Dr. Guoyong Wen
NASA/Goddard Space Flight Center Code 613 & GESTAR/Morgan State University
Greenbelt, MD 20771
Guoyong.Wen-1@nasa.gov
Phone: (301) 614-6220
Fax: (301) 614-6307

Dr. Alexander Marshak
NASA Goddard Space Flight Center, Code 613
Greenbelt, MD 20771
Alexander.Marshak@nasa.gov
(301) 614-6122

Dr. Tamás Várnai
NASA Goddard Space Flight Center, Code 613 &
JCET/University of Maryland Baltimore County
Greenbelt, MD 20771
(301) 614-6408
tamas.varnai@nasa.gov

Dr. Robert Levy
NASA Goddard Space Flight Center, Code 613
Greenbelt, MD 20771
Robert.C.Levy@nasa.gov
(301) 614-6123

ABSTRACT

A transition zone exists between cloudy skies and clear sky, such that clouds scatter solar radiation into clear sky regions. From a satellite perspective, it appears that clouds enhance the radiation nearby. We seek a simple method to estimate this enhancement, since it is so computationally expensive to account for all 3-dimensional (3D) scattering processes. In previous studies, we developed a simple two-layer model (2LM) that estimated the radiation scattered via cloud-molecular interactions. Here we have developed a new model to accounts for cloud-surface interaction (CSI). We test the models by comparing to calculations provided by full 3D radiative transfer simulations of realistic cloud scenes. For these scenes, the MODIS-like radiance fields were computed from the Spherical Harmonic Discrete Ordinate Method (SHDOM), based on a large number of cumulus fields simulated by the UCLA Large Eddy Simulation (LES) model. We find that the original 2LM model that estimates cloud-air molecule interactions accounts for 64% of the total reflectance enhancement, and the new model (2LM+CSI) that also includes cloud-surface interactions accounts for nearly 80%. We discuss the possibility of accounting for cloud-aerosol radiative interactions in 3D cloud induced reflectance enhancement, which may explain the remaining 20% of enhancements. Because these are simple models, these corrections can be applied to global satellite observations (e.g. MODIS) and help to reduce biases in aerosol and other clear-sky retrievals.

1. INTRODUCTION

A transition region exists between clouds and cloud-free air [*Charlson et al.*, 2007; *Koren et al.*, 2007]. Several recent studies have shown that there are changes in aerosol optical depth (AOD) as well as aerosol particle size in this transition zone [e.g., *Su et al.*, 2008; *Loeb and Schuster*, 2008; *Tackett and Di Girolamo*, 2009; *Twohy et al.*, 2009; *Redemann et al.*, 2009;

Jeong and Li, 2010; *Várnai and Marshak*, 2011, 2012, 2014; *Bar-Or et al.*, 2012; *Yang et al.*, 2014]. The transition zone is also a region where solar radiative transfer processes become highly 3-dimensional (3D) [*Wen et al.*, 2008; *Kassianov and Ovtchinnikov*, 2008; *Marshak et al.*, 2008; *Yang and Di Girolamo*, 2008].

Sunlight scattered by clouds enhances the reflectance in nearby clear regions. *Wen et al*. [2008] showed that Rayleigh scattering of cloud reflected sunlight is the dominant mechanism for the reflectance enhancement in clear area near clouds. This 3D cloud effect is similar to the adjacency effect [e.g., *Odell and Weinman*, 1975; *Otterman and Fraser*, 1979; *Kaufman*, 1979*; Lyapustin and Kaufman*, 2001], however it is the cloud instead of a bright surface affecting the image. The 3D cloud effects can lead to an apparent "bluing" of clear region [*Marshak et al.*, 2008] because of larger Rayleigh scattering in shorter wavelengths. In terms of aerosol retrieval, the enhanced radiation not only creates bias in retrieving total AOD but also biases in retrieving spectral dependence and interpreting relative aerosol size (via Ångstrom Exponent). Not accounting for cloud 3D effects will cause incorrect interpretation of satellite-based aerosol data near clouds and hence in accurately quantifying aerosol radiative effects or aerosol-cloud interactions.

In an earlier study [*Marshak et al.*, 2008], we developed a simple two-layer model (2LM) for estimating and correcting for near-cloud enhancement. This 2LM accounted for the radiative interactions between boundary-layer clouds and the molecular layer of clear air above it. This 2LM was "validated" for a few scenes using Monte Carlo calculations [*Wen et al.*, 2007, 2008], which led to *Wen et al.* [2013] applying the correction model to a full Moderate Resolution Imaging Spectroradiometer (MODIS) granule. In this case, *Wen et al.,* [2013] corrected for cloud-molecular interactions in the MODIS bands, and the "corrected" reflectances were then

used as inputs for the dark-target MODIS aerosol retrieval [*Remer et al.*, 2005; *Levy et al.*, 2010].

It is not clear whether the simple 2LM always improves MODIS aerosol retrievals. Since Rayleigh scattering optical depth decreases much faster with wavelength (inversely proportional to the 4^{th} power of wavelength) than does either AOD or ocean spectral albedo, corrections only for cloud-Rayleigh interactions may lead to a different kind of bias. At longer wavelengths, where Rayleigh scattering is negligible, aerosol scattering and ocean reflection can be substantial, especially under coarse-size aerosol or rough ocean conditions. Thus the corrections for Rayleigh scattering alone skew towards shorter wavelengths [*Wen et al.*, 2013] and bias aerosol retrieval.

Recently, *Marshak et al.* [2014] developed a new approach to overcome the shortcoming of the 2LM by relating the short wavelength (e.g., 0.47 μm of MODIS) correction to longer wavelengths. They found that the reflectance and the enhancements for the longer wavelength were linearly correlated with to the 0.47μm band. More importantly, the linear regression coefficient (i.e., the slope) relating the reflectance enhancement for a longer wavelength to that for the short wavelength can be approximated by the linear regression coefficient for the reflectances for the same pair of wavelengths. Note that the linear regression coefficients depend on aerosol properties and the surrounding cloud structure and are computed for each MODIS 10 km box. Thus reflectance enhancement at longer wavelengths can be derived from the enhancement at 0.47 μm. In this study, then, we focus on reflectance enhancement at 0.47 μm.

Two essential tasks need to be carried out in order to make the correction model as a useful tool for MODIS aerosol retrievals. First, we need to reduce the bias of the 2LM alone by including other 3D cloud radiative effects in addition to cloud-Rayleigh scattering interaction.

Second, we need to test the correction model to quantify errors in the reflectance enhancement estimates.

In this paper, we present a new model that estimates the reflectance enhancements due to cloud-surface interactions. We perform an error analysis to the models by comparing the model-estimated reflectance enhancements to the truth computed by the Spherical Harmonic Discrete Ordinate Method (SHDOM) [*Evans*, 1998] for a large number of cumulus cloud fields generated from UCLA Large Eddy Simulation (LES) model [*Stevens et al.*, 1999] and GEOS-5 aerosol profiles. This approach is similar to those of *Yang and Di Girolamo* [2008] and *Marshak et al.* [2014] in studying 3D radiative effects for satellite remote sensing.

Section 2 briefly reviews the 2LM and presents the method of accounting for cloud-surface interactions. The data of LES/SHDOM simulations are described in section 3. The error analyses are presented in Section 4, along with discussion of the possibility to account cloud-aerosol radiative interactions, which is followed by a summary section.

2. Two Models for Clear Sky Enhancement due to Nearby Clouds

Sunlight scattered by broken clouds enhances diffuse solar radiation in the clear area in the vicinity of clouds. Subsequent scattering of the diffuse sunlight by air molecules, aerosols, and surface leads to the enhancement of clear column reflectance. 3D clouds also cast shadows to decrease the reflectance in nearby clear areas [e.g., *Di Giuseppe and Tompkins*, 2003], and methods have been developed to discriminate cloud shadows for MODIS remote sensing [e.g., *Ackerman et al.*, 1998; *Remer et al.*, 2005]. In this paper, we consider only the enhancement effects of clouds. We first briefly review the 2LM developed earlier for correcting clear-air reflectance enhancement due to cloud-air molecule interactions [*Marshak et al.*, 2008]. Then we present a method for also accounting for cloud-surface radiative interactions.

2.1. THE TWO-LAYER MODEL (2LM) FOR CLOUD-AIR MOLECULE INTERACTIONS

Fig. 1a sketches the 2LM that estimates clear-air reflectance enhancement due to the radiative interactions between a cloud layer with cloud albedo α_c and the overlaying molecular atmosphere with scattering optical depth of τ_m. In this model, the clear-air reflectance enhancement is the result of cloud-reflected upward radiation being scattered by the molecular layer into the direction of the satellite sensor.

In the two-layer system, we consider the processes that affect radiation reflected from clouds as it travels through the molecular layer above. These radiative transfer processes include scattering and extinction by air molecules, and multiple reflections between the cloud layer and the molecular layer above it. To derive an analytical approximation for the cloud-induced reflectance enhancement, we consider two reflectances for the two-layer system. One is the reflectance from a broken cloud field with a scattering molecular layer above it. This reflectance includes both scattered radiation and cloud reflected radiation attenuated by molecular scattering. The other is second component in the first reflectance (i.e., the reflected radiation from the same broken cloud field but with the molecules in the upper layer causing extinction) [*Marshak et al.*, 2008]. The difference between the two reflectances yields the reflectance scattered to the sensor, or the reflectance enhancement. Both reflectances may be expressed analytically as described below.

Generated by the cloud reflected upward flux, the first reflectance (r_1) is simply the total TOA reflectance that includes molecular scattering, extinction, and multiple reflections between two layers. Generated by the same upward flux, the second reflectance (r_2) is the non-scattered radiance with the molecular layer causing only extinction. The expressions for the two reflectances are shown in Eq. (1):

$$r_1(\lambda,\Omega,\Omega_0)=\frac{\alpha_c T_m(\tau_m(\lambda),\Omega_0)T_{m,diff}(\tau_m(\lambda),\Omega)}{1-\alpha_c R_m(\tau_m(\lambda))}, \quad (1a)$$

$$r_2(\lambda,\Omega,\Omega_0)=\frac{\alpha_c T_m(\tau_m(\lambda),\Omega_0)T_{m,beam}(\tau_m(\lambda),\Omega)}{1-\alpha_c R_m(\tau_m(\lambda))}. \quad (1b)$$

where α_c is cloud albedo, $\tau_m(\lambda)$ is the molecular scattering optical depth above cloud top level for wavelength λ, $\mathbf{\Omega_0}$ and $\mathbf{\Omega}$ are the directions to the Sun and the satellite, T_m and $T_{m,diff}$ are transmittances of the molecular layer for collimated sunlight from above and diffuse radiation reflected from the cloud layer below, respectively, R_m is the reflectance of the molecular layer for upwelling radiation from the cloud layer, and $T_{m,beam}= \exp(-\tau_m(\lambda)/\mu)$ is the beam transmittance of the molecular layer for upwelling radiation from the cloud layer, where μ is the cosine of the satellite viewing zenith angle (VZA). (See Table I in *Wen et al.*, 2013, for the detailed definition of each term.)

The difference between the two reflectances gives the molecule-scattered reflectance in the two-layer system or cloud-induced reflectance enhancement (ΔR_m), as shown in Eq. (2)

$$\Delta R_m(\lambda,\Omega,\Omega_0)=\frac{\alpha_c T_m(\tau_m(\lambda),\Omega_0)}{1-\alpha_c R_m(\tau_m(\lambda))}\left[T_{m,diff}(\tau_m(\lambda),\Omega)-T_{m,beam}(\tau_m(\lambda),\Omega)\right]. \quad (2)$$

Fig. 1b shows schematically the characteristics of the 2LM versus the real enhancement. For a given viewing angle, the reflectance enhancement is approximately a linear function of the 1D cloud albedo α_c since the contribution from multiple reflections is small (see Eq. (2)). As we will see in Section 4, the true enhancement is not a linear function of 1D cloud albedo; it increases quickly for small cloud albedos and gradually saturates for large cloud albedos. For small cloud albedos, the 2LM underestimates the truth because it does not account for cloud-surface and cloud-aerosol interactions. For large cloud albedos, the 2LM enhancement estimates continue to increase linearly with cloud albedo, which overestimates the non-linear (saturated) enhancement.

The input for the 2LM includes cloud scene albedo, molecular optical depth above clouds, solar zenith angle (SZA), and satellite viewing geometry. The average cloud scene albedo in each 10 km x 10 km box is estimated using the plane-parallel independent pixel approximation (IPA) by averaging the albedo for each 500 m pixel computed using cloud optical depths provided in LES/SHDOM simulation data. The transmittances and reflectance of the molecular layer are calculated as a function of the known cloud-top height. In practice, cloud albedo may be estimated using broadband to narrowband conversion method [*Wen et al.*, 2013], and MODIS cloud-top height [*Platnick et al.*, 2003] can be used to compute molecular layer reflectance and transmittances.

2.2. CLOUD-SURFACE RADIATIVE INTERACTIONS (CSI)

Sunlight scattered by broken clouds increases the downward diffuse radiative flux in nearby clear areas and subsequently leads to the reflectance enhancement through surface reflection and atmospheric extinction. Thus the reflectance enhancement (ΔR_s) due to cloud-surface radiative interactions (CSI) may be expressed as

$$\Delta R_s = T_{clear}\alpha_s e^{-\frac{\tau}{\mu}}, \qquad (3),$$

where T_{clear} is the cloud-induced clear area diffuse transmittance (i.e., the extra radiation that reaches a surface area because of sideways scattering by clouds), α_s the surface albedo, τ the atmospheric optical depth (aerosol and molecular scattering), μ the cosine of VZA.

Here, we use a one-layer, stochastic Poisson model to model the downward diffuse radiative flux from a broken cloud field [*Titov*, 1990; *Kassianov*, 2003; *Zhuravleva and Marshak* 2005]. The second simulation of satellite signal in the solar spectrum (6S) model [*Vermote et al.*, 1997], the same one used for SHDOM simulation, is used to compute surface albedo. The Poisson

model [*Titov*, 1990] assumes that for a given cloud fraction clouds are distributed uniformly in a unit volume. For statistically homogeneous cloud fields, a closed system of equations is derived for average intensity, and the closed equations are solved using Monte Carlo method. While this Poisson model can be generalized to multi-layers [e.g., *Kassianov*, 2003], and compared with fractal cloud model for radiative flux computation [*Zhuravleva and Marshak*, 2005], we use the one-layer Poisson model in this study.

The Poisson model is completely determined by cloud fractional cover (f), cloud geometric thickness H, average horizontal size of clouds D, and averaged cloud optical properties, including cloud optical depth, single scattering albedo and scattering phase function. For a fixed cloud thickness the cloud aspect ratio defined as the ratio of cloud horizontal to vertical extent (D/H) is used as input parameter. For given inputs of cloud properties and solar zenith angle, the Poisson model computes the domain average albedo, absorption, and transmittances for both direct and diffuse radiation.

To calculate cloud-induced diffuse transmittance, we use the following approximation. First, we assume that the domain average diffuse transmittance ($T_{3D,cloudy}$) is a fractional area-weighted sum of clear and cloudy diffuse transmittances (T_{clear} and T_{cloud}),

$$T_{3D,cloudy} = fT_{cloud} + (1-f)T_{clear} \tag{4}$$

where $T_{3D,cloudy}$ is computed by the stochastic Poisson model for a broken cloud field and T_{cloudy} is computed from the plane parallel approximation. From here the clear sky diffuse transmittance can be estimated as

$$T_{clear} = \left(T_{3D,cloudy} - fT_{cloud}\right)/(1-f)\,. \tag{5}$$

Assuming a cloud aspect ratio of 2, Fig. 2 plots the Poisson model-computed clear-sky diffuse transmittance as a function of broken cloud field albedo. Each point represents a different

190 cloud fraction and average cloud optical depth (COD). There are some notable distinctive
191 features. For a given cloud fraction, the diffuse transmittance increases rapidly with for small
192 CODs, reaches local maxima, and then decreases gradually. For a given cloud optical depth, the
193 diffuse transmittance increases with cloud fraction, reaching 0.25-0.30 for a broken cloud field
194 albedo greater than 0.25.

195 We have run the Poisson model for a discrete values of cloud properties and solar
196 geometries, thus creating lookup tables (LUTs) of diffuse transmittance. Together with the ocean
197 albedo computed from the ocean reflection model and atmospheric extinction, we are able to
198 estimate the enhancement due to cloud-surface radiative interaction.

199 **3. DATA**

200 Our study considers the radiation fields for cumulus cloud scenes over oceans. LES model
201 was used to generate 26 cumulus cloud fields. Initialized using meteorological profiles
202 (temperature, water vapor, wind components and vertical velocity) from the ERA-Interim
203 reanalysis [*Dee et al.*, 2011], the LES runs were performed with a domain size of 20 km x 20
204 km, with a horizontal grid spacing of 62.5 m and a variable vertical grid with 59 to 102 levels
205 with vertical resolution of 40 m or less. Each simulation started at 06:00 local time and lasted for
206 8 hours. The LES cloud microphysics assumes a fixed cloud droplet concentration and uses a
207 two-moment drizzle/rain bulk microphysics scheme. The cloud droplet concentration was chosen
208 randomly from an exponential distribution between 40 cm^{-3} and 400 cm^{-3}. The LES shortwave
209 and longwave radiative cooling/heating rates were calculated using the Fu/McISA [*Pincus and*
210 *Stevens*, 2009] independent column approximation radiative transfer code. An example of LES
211 cloud optical depth field and computed 1D albedo is presented in Fig. 3.

212 For 3D radiative computation, the cloud field for a single time (6 hr or 12:00 pm local time)

213 was chosen for each of the 26 LES simulation. Fig. 4a show cloud properties of the 26 LES
214 clouds. The 26 LES cloud fields were combined with 40 representative aerosol profiles. Out of
215 26 LES cloud fields, 24 fields were combined with 3 different aerosol profiles, and 2 fields with
216 4 different aerosol profiles to make 80 different cloud/aerosol scenes. In other words, each of the
217 40 aerosol profiles was used with two different cloud scenes to make 80 different cloud/aerosol
218 scenes.

219 These aerosol profiles were obtained from GEOS-5 [*Rienecker et al.*, 2011] global fields
220 over tropical and mid-latitude oceans. GEOS-5 has five aerosol types: dust, sea salt, sulfate,
221 black carbon, and organic carbon [*Chin et al.*, 2002; *Colarco et al.*, 2010]. Aerosol optical
222 properties were calculated from the GEOS-5 optical property tables as a function of LES relative
223 humidity. Thus aerosol optical properties vary horizontally and vertically in space. The 40
224 aerosol profiles have a wide range of aerosol properties as shown in Fig. 4b.

225 The radiances for these 80 scenes were calculated with SHDOM at the LES resolution for the
226 seven MODIS bands used for aerosol remote sensing (wavelengths of 0.466, 0.553, 0.646,
227 0.855,1.243, 1.632, and 2.119 μm) [*Remer et al.*, 2005]. Rayleigh molecular scattering and
228 molecular absorption from water vapor and ozone were included up to the 15.6 km domain top.
229 An SHDOM ocean surface reflectance model with the LES surface wind speed was assumed.
230 The solar-viewing geometry was obtained for the LES latitude, date, and the 13:30 local time of
231 the Aqua overpass. SHDOM runs were made for 3D cloud/aerosol fields (i.e., MODIS-like), 3D
232 hydrated aerosol-only fields, and 1D aerosol-only fields. For 3D cloud/aerosol fields and 3D
233 hydrated aerosol-only fields, aerosol optical properties respond to the LES relative humidity
234 through aerosol hydration and vary horizontally and vertically in space. For 1D aerosol-only
235 fields, the horizontally averaged outside-cloud relative humidity is used to compute aerosol

236 optical properties. In this study, the true reflectance enhancement (ΔR_{truth}) is defined as the
237 difference between reflectances for the 3D cloud/aerosol fields and the 3D hydrated aerosol-only
238 fields.

239 The standard MODIS aerosol retrieval [*Levy et al.*, 2013] uses input observations at 500 m
240 spatial resolution (nominal at nadir view) to derive aerosol properties at 10 km resolution.
241 Therefore, we averaged the SHDOM results (the 3D cloud/aerosol reflectance fields for cloudy
242 and the 3D hydrated aerosol-only reflectance fields for clear) to provide 500 meter resolution
243 MODIS-like data in the seven wavelengths. To account for the variability of global observing
244 geometry, these values were calculated for 23 viewing directions with zenith angles every 6°
245 from 0° to 66°. Note, that the upper bound in the model configuration is 15 km, rather than 700
246 km observation of MODIS. Within scene (20 km x 20 km) variation in viewing and solar angles
247 are ignored. Thus for each MODIS band, there are 1840 (80 cloud/aerosol scenes times 23
248 viewing directions) radiance images. These scenes would be broken into 10 km x 10 km boxes of
249 500 m pixels, following the strategy of the MODIS aerosol retrieval.

250 The MODIS aerosol retrieval performs upon clear (non-cloud) pixels. Following the cloud-
251 masking scheme of operational MODIS dark target aerosol retrievals [*Martins et al.*, 2002;
252 *Remer et al.*, 2005; *Levy et al.*, 2010], we identified clear pixels within each 10 km x 10 km box
253 of each of the 1840 MODIS-like cloud/aerosol scenes. Overall, 100188 of the 500 m pixels and
254 associated 3154 of the 10 km boxes passed the test. Note that more clear pixels passed MOD04
255 test for nadir viewing direction than that for oblique viewing angles (Fig. 2c), and that the Aqua
256 satellite has a local equatorial crossing time approximately 1:30 pm. Therefore, the results in this
257 study are biased slightly towards higher sun and lower viewing zenith angles.

4. RESULTS

We test our models by comparing the estimated reflectance enhancements to the truth. We test (1) the 2LM that accounts for cloud-molecule radiative interactions to estimate ΔR_m, and (2) the 2LM+CSI that accounts for cloud-molecule and cloud-surface radiative interactions to estimate $\Delta R_m+\Delta R_s$. First we show an example of 2LM. Then we present results for the two models, followed by a discussion of possibility to account for cloud-molecule, cloud-surface, and cloud-aerosol radiative interactions in a model called 2LM+CSI+CAI.

4.1. AN EXAMPLE FOR 2LM

We compared 2LM with the truth for the cloud field in Fig. 3a as an example. Fig. 5 shows the view-angle dependence of reflectance enhancements for the four 10 km x 10 km sub-images of the cloudy scene in Fig. 3a. The true reflectance enhancements are in color, and those for 2LM are in black. A distinctive feature of the true reflectance enhancement is its view-angle dependence. It is evident that the true reflectance enhancement increases with view angle, and that 2LM also captures, to some extent, this dependence.

Another remarkable feature of the 2LM is that its reflectance enhancements for the four 10 km x 10 km boxes are very different from one another. This is due primarily to the dependence of the 2LM reflectance enhancement on cloud albedo, for cloud-top height is less variable for cumulus clouds (see Eq. (2)). Starting counter-clockwise from the upper left corner (Fig. 5a), the increase of average 2LM enhancement (0.0028, 0.0045, 0.0049, 0.0069 in Fig. 5) is evidently associated with increase in cloud field albedo (0.05, 0.07, 0.08, 0.12 in Fig. 3b).

Unlike the 2LM enhancement, the true reflectance enhancement does not have a clear dependence on the 1D cloud albedo because, in reality, it is a result of a non-linear 3D radiative transfer interaction between cloud and clear air. The true scene albedo of a 10 km x 10 km box is

not a unique function of cloud optical properties either, and is strongly affected by cloud-field structure [*Marshak et al.,* 1995]. Furthermore, the true enhancement calculations also account for the hydrated aerosols that vary in 3D space. As a result, the true reflectance enhancement is more variable than its 2LM counterpart.

The errors in 2LM reflectance enhancement for each 10 km x 10 km box vary from scene to scene, and can be relatively large and view angle dependent. For example, for the two boxes on the right side of Fig. 3a, the error is about 10%. However, for the upper-left box in Fig. 3a, the error ranges from -0.003 (-50%) for nadir direction to -0.006 (-60%) for the oblique viewing angle of 48° (black dots minus colors in Fig. 5a). For the 20 km x 20 km domain and viewing angle average, the error in 2LM enhancement is about -31%, which differs tremendously form the error for each 10 km x 10 km boxes. Thus, it is important to compare the statistics of modeled reflectance enhancements to the truth, as described in the following sections.

4.2. 2LM FOR CLOUD-AIR MOLECULE INTERACTIONS

Figure 6 compares the 2LM reflectance enhancements with the true enhancement values for different view angles for all scenes as a function of 1D cloud scene albedo. It is clear that both modeled and the true reflectance enhancements increase with cloud albedo for a given viewing angle. However, there are some remarkable differences between the two as the sketched in Fig. 1b. As expected from Eq. (2), for a given view-angle, the 2LM reflectance enhancement is a linear function of cloud albedo. In reality, the enhancement is a non-linear function of the 1D cloud albedo. The true enhancement increases rapidly for small cloud albedos, and saturates at the larger ones. The true enhancement is always larger and more variable than its model counterpart for albedos smaller than 0.15. However, for albedos larger than 0.15, for some cases the true enhancement is smaller than its 2LM estimate.

304 The 2LM underestimates the true enhancement at least for albedo smaller than 0.15 because
305 it lacks contributions from cloud-surface and cloud-aerosol radiative interactions. The
306 overestimate of the enhancement for large 1D cloud albedos is primarily the result of the
307 application of the simple linear model to situations when the non-linearity of radiative transfer is
308 pronounced. This also suggests the limitation of the 2LM for larger cloud albedos or cloud
309 optical depth and cloud fraction.

310 Fig. 7a compares the average and standard deviation of 2LM estimated reflectance
311 enhancements with the truth as a function of cloud scene albedo. There are 104 different albedo
312 values and 3154 radiances for 10 km x 10 km boxes. The latter is the result of the same number
313 of broken cloud scenes with different combinations of aerosol profiles and viewing angles. Thus
314 there are 104 average reflectance enhancements corresponding to each individual cloud albedo,
315 for both 2LM and the truth. The error bars show the standard deviation of scene-average
316 enhancement values due to different view direction for 2LM and additional variation in aerosol
317 properties for the truth.

318 Similar to those for different VZA in Fig. 1b and Fig. 6, both modeled and true average
319 reflectance enhancements increase with cloud albedo. The 2LM average reflectance
320 enhancement increases rather linearly while the true average enhancement has a much bigger
321 dynamic range for each value of cloud field albedo. Again, we clearly see that 2LM
322 underestimates the true enhancement at least for albedo smaller than 0.15.

323 The standard deviation of 2LM reflectance enhancement for a given cloud albedo is much
324 smaller than the truth. This is because, for a given cloud field, the 2LM reflectance enhancement
325 only varies with viewing angle, while the true enhancement, in addition to viewing geometry,
326 depends on the 3D radiative transfer process and variable aerosol properties. As a result, the

mean values of the 104 average enhancements and the standard deviations are smaller for the 2LM (0.0038 and 0.0003, respectively) than that for the truth (0.0055 and 0.0009, respectively). On average, the cloud-air molecule interaction accounts for about 70% of the 3D enhancement, which is consistent with the results of *Wen et al.* [2008]. In other words, the 2LM reflectance enhancement is biased low by 30%.

Next we compare the averages and standard deviation of the 2LM enhancements with the truth for different mean cloud optical depths (Fig. 7b) and different cloud fractions (Fig. 7c). There are 317 unique average cloud optical depths and 88 different cloud fraction values. For both 2LM and the truth, the average enhancement increases with average cloud optical depth and cloud fraction. This is similar to Fig. 7a because cloud scene albedo, average cloud optical depth, and cloud fraction are positively correlated. Compared to the true values, the 2LM average enhancement increases more linearly with either cloud optical depth or cloud fraction. Similarly to Fig. 7a, the model underestimates the mean and standard deviation of the enhancements except for a few cases for large enough cloud optical depths and cloud fractions.

It is important to note that the 2LM already overestimates the enhancement for large cloud field albedos (cloud optical depth, and/or cloud fraction). The critical values of cloud albedo (0.1) and cloud fraction (0.6) were determined empirically; no further correction for cloud-surface radiative interactions will be made for cloud fields with an albedo higher than 0.1 or cloud fraction larger than 0.6 in 2LM+CSI.

4.3. 2LM+CSI FOR CLOUD-AIR MOLECULE AND CLOUD-SURFACE RADIATIVE INTERACTIONS

2LM accounts about 70% of the true reflectance enhancement. Here we show that the 2LM can be further improved when additional cloud-surface interactions are included in 2LM+CSI.

Similar to Fig. 7a, Fig. 8a compares the enhancements for 2LM+CSI as a function of cloud field albedo. It is clear that including cloud-surface interactions improves the model estimates of the reflectance enhancement for cloud field albedos less than 0.1. For 2LM+CSI, the mean value of average reflectance enhancement is 0.0046 compared to 0.0038 for 2LM. As a result, the 2LM+CSI (cloud-air molecule and cloud-surface interactions) accounts for 84% of the true enhancement of 0.0055. The bias in 2LM+CSI is about 16% compared to 30% for 2LM. Note the 2LM+CSI does not change the typical standard deviation. The comparison between the 2LM+CSI and the true enhancements as a function of cloud optical depth and cloud fraction is also shown in Figs. 8b and 8c, respectively.

The improvement of the models may be seen from scatter plots in Fig. 9, with different cloud fractions indicated by colors. As expected, the model-estimated enhancement increases with cloud fraction. Note that 2LM+CSI does not apply to cloud fields with cloud fractions bigger than 0.6. Straight lines are fitted to the scatter plot through the origin. Evidently, the slope increases from 0.58 for 2LM, to 0.73 for 2LM+CSI, showing the improvement when cloud-surface radiative interactions are accounted for in the 2LM.

4.4. Statistical Distributions of Errors in Model Estimates

Finally, we examine the error distribution in the model-estimated reflectance enhancements. In the error distribution for 2LM (Fig. 10a), the median, mean, and standard deviation are -0.0013, -0.0018, and 0.0017, respectively. The majority of the differences between the 2LM enhancement values and the true ones are negative and only 4% of values are positive. Comparing with the average true reflectance enhancement of 0.00496 (Fig. 11), we find that overall average of 2LM is biased low by about 36%, slightly more than they were for different

371 cloud properties in Figure 7. Also, the magnitude of the standard deviation is as large as the
372 magnitude of the mean value.

373 The error distribution for 2LM+CSI (Fig. 10b) has a median, mean, and standard deviation of
374 -0.0007, -0.0010, and 0.0015, respectively. In the distribution, 23% of values are greater than
375 zero, compared with 4% for 2LM. From 2LM to 2LM+CSI, overall statistical bias error reduced
376 by half from -0.0018 to -0.0010. The standard deviation is slightly smaller for 2LM+CSI than for
377 2LM. The bias error is reduced from -36% for 2LM to -20% for 2LM+CSI.

378 Fig. 11 compares the frequency distribution of 2LM+CSI estimated reflectance enhancement
379 with the truth. We find that the frequency distribution for 2LM+CSI largely resembles that for
380 the truth. The median, mean, and standard deviation for 2LM+CSI are 0.00315, 0.00390, and
381 0.00234 compared to 0.00418, 0.00496, and 0.00301 for the truth. For overall statistics, the
382 2LM+CSI accounts for ~80% of the enhancement.

383 **4.5. DISCUSSION OF CLOUD-AEROSOL INTERACTIONS**

384 Similarly to cloud-surface radiative interactions, cloud-induced diffuse radiation scattered by
385 aerosol also enhance clear column reflectance. However, the reflectance enhancement (ΔR_a) due
386 to cloud-aerosol radiative interactions is much more difficult to estimate, since the enhancement
387 not only depends on the cloud-induced diffuse radiation but also on unknown aerosol properties;
388 moreover, it depends on the unknown distribution of scattering angle in the process of radiative
389 interactions between clouds and aerosols. Still, the contribution of cloud-aerosol radiative
390 interactions may be approximately estimated. Here we show that the concept of the 2LM
391 developed for cloud-air molecule radiative interactions can also be useful for estimating cloud-
392 aerosol interactions.

Consider the top layer in the 2LM consisting of air molecules and aerosols. We cannot simply include aerosol effects by adding AOD to the molecular optical depth in the 2LM because the aerosol scattering phase function is much more variable than that for molecular scattering, and strongly depends on the unknown scattering angle. In order to somehow account for aerosols in the 2LM, we can use the single scattering approximation.

We consider the reflectance for a layer consisting of molecules and aerosols. In a single scattering approximation, the reflectance is proportional to optical depth, single scattering albedo, and scattering phase function, i.e.

$$r(\theta,\theta',\phi-\phi') = \tau_m P_m(\mu_{scat})/(4\mu\mu') + \omega_a\tau_a P_a(\mu_{scat})/(4\mu\mu'). \quad (6)$$

Here τ_m and P_m are molecular optical depth and scattering phase function, ω_a, τ_a, P_a are aerosol single scattering albedo, optical depth and scattering phase function, μ=cos(θ) and μ'=cos(θ') are cosines of the viewing and incident zenith angles (θ and θ'), ϕ and are ϕ' are azimuth angles, and μ_{scat} is cosine of the effective scattering angle [*Hansen and Travis*, 1974; *Kaufman et al.*, 1997]. Eq. (6) may also be expressed as

$$r(\theta,\theta',\phi-\phi') = \tau_{m,eff} P_m(\mu_{scat})/(4\mu\mu'), \quad (7a)$$

where the effective molecular scattering optical depth $\tau_{m,eff}$ is

$$\tau_{m,eff} = \tau_m + \varepsilon\tau_a \quad (7b)$$

and

$$\varepsilon = \omega_a P_a(\mu_{scat}) / P_m(\mu_{scat}). \quad (7c)$$

The scale factor ε accounts for the phase function difference between molecular and aerosol scattering at the μ_{scat}. Thus one can get a rough estimate of the total enhancement due to cloud-

414 aerosol and cloud-air molecule radiative interactions using the same molecular scattering
415 equation by adding a scaled optical depth to the molecular optical depth.

416 Figure 12 shows the phase function ratios for the 40 aerosol types. The phase function ratio
417 has a peak in the forward direction. The ratio is less than one for a large range of scattering
418 angles and has minimum value around 0.1-0.2. To demonstrate the possible magnitude of
419 reflectance enhancement contributions from cloud-aerosol interactions, we use the AOT values
420 provided in the data set and assume a small value of 0.2 for ε. The result is presented in Fig. 13.
421 Note that, similarly to 2LM+CSI, the enhancement due to cloud-aerosol interactions induced
422 enhancement is not computed for cloud field albedos larger than 0.1 or for cloud fraction larger
423 than 0.6. The figure shows that the 2LM including additional cloud-aerosol radiative interactions
424 can accounts for 90% of the enhancement for this somewhat arbitrary small ε.

425 Here we used a somewhat arbitrary ε and AOT values in the data set to demonstrate a rough
426 magnitude of the reflectance enhancement due to cloud-aerosol interactions. In real application,
427 Monte Carlo simulations could provide the parameter ε as a function of aerosol and cloud
428 properties and Sun-view geometry, and the MODIS retrieved AOT may be used as a first
429 approximation for estimating the enhancement.

430 **5. SUMMARY AND DISCUSSION**

431 We developed a new model to account for cloud-surface interactions that make significant
432 contributions to clear sky reflectance enhancements in broken cloud fields. In the new method,
433 the cloud-surface radiative interactions are accounted for by using an existing Poisson model of
434 cloud spatial distribution [*Titov*, 1990] to estimate cloud-induced downward diffuse radiative
435 flux at the surface. The radiative transfer computation for Poisson cloud fields is efficient to
436 provide sufficiently accurate domain average fluxes [*Zhuravleva and Marshak*, 2005]. This

437 model can be applied for operational processing for correcting reflectance enhancement due to
438 cloud-surface radiative interaction for MODIS aerosol retrieval.

439 We further assessed the accuracy of two models. The first one is the 2LM that accounts only
440 for cloud-air molecule radiative interactions. The second model, or 2LM+CSI, accounts for both
441 cloud-air molecule and cloud-surface radiative interactions. We tested these models to quantify
442 errors in the reflectance enhancement estimates using the true radiances calculated by SHDOM
443 [*Evans*, 1998] for 80 cloud/aerosol scenes from LES [*Stevens et al.*, 1999]. We demonstrated that
444 the true reflectance enhancement has clear view angle dependence, and that 2LM (the model that
445 accounts for cloud-air molecule interactions only) captures much of this dependence. While the
446 2LM enhancement for each individual image may have large errors, on average 2LM results are
447 reasonable.

448 Detailed analyses show that, for a given viewing angle, 2LM estimated enhancement
449 increases linearly with the 1D cloud field albedo. The true enhancement increases nonlinearly
450 with the cloud field albedo: it increases rather quickly for small albedos and then becomes
451 saturated for large albedos. The 2LM enhancements are smaller and less variable compared to
452 the truth except for a few cases with large cloud albedos, cloud optical depth, or cloud fractions
453 indicating the limitation of the 1D model for those clouds. The mean error of 2LM for average is
454 -36%.

455 We performed detailed analysis to the reflectance enhancement from the model that accounts
456 for both cloud-air molecule and cloud-surface interactions (2LM+CSI). We found that the mean
457 value of the enhancement increased from 64% of the true value for 2LM to 80% for 2LM+CSI.
458 In other words, the mean error is reduced from -36% for 2LM to -20% for 2LM+CSI. Thus,

459 including cloud-surface radiative interactions in 2LM+CSI has made significant improvement to
460 the 2LM.

461 It is important to note that the 2LM is a simple model. It uses the plane-parallel
462 approximation to compute cloud albedos used for estimating the reflectance enhancements due to
463 cloud-air molecule interactions. In reality, cloud albedo in a 10 km x 10 km box is not a unique
464 function of its optical properties and can also be affected by clouds in neighboring boxes.
465 Without considering 3D radiative transfer, the plane-parallel assumption can introduce large
466 errors in estimating albedo and associated reflectance enhancement for a given cloudy scene. On
467 average, however, the model performed reasonably well estimating the true enhancement when
468 only cloud-air molecular radiative interactions are accounted for.

469 Similarly, the stochastic Poisson model is expected to provide statistically accurate fluxes.
470 For a given cloudy scene, however, the model may have large errors due to both the stochastic
471 nature of the model and the plane-parallel assumption used in deriving the clear sky diffuse flux.
472 However, the error in surface-associated reflectance enhancement is expected to be small
473 compared to that due to the plane-parallel assumption in computing 2LM reflectance
474 enhancement because cloud-surface interaction is not the largest contribution to the reflectance
475 enhancement. Nevertheless, the Poisson model is efficient in estimating the clear sky downward
476 diffuse flux needed for computing the enhancement due to cloud-surface radiative interactions.

477 We have discussed the possibility of accounting for cloud-aerosol interactions in the 2LM.
478 We demonstrated that the bias in enhancement estimate may be further reduced by introducing
479 an effective molecular optical depth for cloud-aerosol radiative interactions and using a
480 somewhat arbitrary parameter ε. Here we used AOT values provided in our data set. In reality
481 the AOT may be estimated using MODIS product as a first order approximation. The parameter

482 ε may be empirically estimated using aerosol information obtained from satellite observation and
483 Monte Carlo simulations.

484 This study focuses on the 2LM for the MODIS aerosol band at 0.47 μm. In contrast,
485 operational MODIS aerosol retrievals rely on spectral reflectances measured at seven
486 wavelengths. Recently, a new method was developed to relate the enhancement at a short
487 wavelength to those at longer wavelengths [*Marshak et al.*, 2014]. Combining the 2LM for a
488 short wavelength such as 0.47 μm with the method for longer wavelengths, we plan to perform
489 further analysis to assess errors in 2LM estimates of spectral reflectance enhancements, and to
490 test the way using these two models would affect MODIS aerosol retrievals.

491 *Acknowledgments*. This research is supported by funds provided by the NASA EOS program.

492 **REFERENCES**

493 Ackerman, S. A., K. I. Strabala, W. P. Menzel, R. A. Frey, C. C. Moeller, and L. E. Gumley
494 (1998), Discriminating clear sky from clouds with MODIS, *J. Geophys. Res.*, 103(D24),
495 32,141–32,157, doi:10.1029/1998JD200032.

496 Bar-Or, R. Z., I. Koren, O. Altaratz, and E. Fredj (2012), Radiative properties of humidified
497 aerosols in cloudy environment, *Atmos. Res.*, 118, 280–294.

498 Charlson, R. J., A. S. Ackerman, F. A-M. Bender, T. L. Anderson, and Z. Liu (2007), On the
499 climate forcing consequences of the albedo continuum between cloudy and clear air, *Tellus*,
500 **59**, 715-727.

501 Chin, M., P. Ginoux, S. Kinne, O. Torres, B.N. Holben, B.N. Duncan, et al. (2002), Tropospheric
502 aerosol optical thickness from the GOCART model and comparisons with satellite and
503 sunphotometer measurements, *J. Atmos. Sci.*, 59:461–83.

504 Colarco, P., A. da Silva, M. Chin, T. Diehl (2010), Online simulations of global aerosol
505 distributions in the NASA GEOS4 model and comparisons to satellite and ground-based
506 aerosol optical depth, *J. Geophys. Res.*, 115:D14207.
507 Dee, D.P. et al. (2011), The ERA-Interim reanalysis: configuration and performance of the data
508 assimilation system, *Q. J. R. Meteorol. Soc.* **137**: 553–597. DOI:10.1002/qj.828.
509 Di Giuseppe, F., and A. M. Tompkins (2003), Three-dimensional radiative transfer in tropical
510 deep convective clouds, *J. Geophys. Res.*, 108(D23), 4741, doi:10.1029/2003JD003392.
511 Evans, K. F. (1998), The Spherical Harmonics Discrete Ordinate Method for Three-Dimensional
512 Atmospheric Radiative Transfer, *J. Atmos. Sci.*, **55**, 429-446.
513 Hansen, J. E. and L. Travis (1974), Light scattering in planetary atmosphere, *Space Science*
514 *Reviews*, **16**, 527-610.
515 Jeong, M. J. and Z. Li (2010), Separating real and apparent effects of cloud, humidity, and
516 dynamics on aerosol optical thickness near cloud edges, *J. Geophys. Res.*, 115, D00K32,
517 doi:10.1029/2009JD013547, 2010.
518 Kassianov, E. (2003), Stochastic radiative transfer in multilayer broken clouds. Part I: Markovian
519 approach, *J. Quant. Spectrosc. Radiat. Transfer*, 77, 373– 394, doi:10.1016/S0022-
520 4073(02)00170-X.
521 Kassianov, E. I., and M. Ovtchinnikov (2008), On reflectance ratios and aerosol optical depth
522 retrieval in the presence of cumulus clouds, *Geophys. Res. Lett.*, 35, L06807,
523 doi:10.1029/2008GL033231.
524 Kaufman, Y. J. (1979), Effect of the Earth atmosphere on contrast for zenith observation, *J.*
525 *Geophys. Res.*, 3165-3172, DOI: 10.1029/JC084iC06p03165.

526 Kaufman, Y.J., D. Tanre, L. Remer, A. Chu, E. Vermote, A. Chu, and B. N. Holben (1997),
527 Operational remote sensing of tropospheric aerosol over land from EOS Moderate Resolution
528 Imaging Spectroradiometer, *J. Geophys. Res.*, *102*, 17051-17067.
529 Koren, I., L. A. Remer, Y. J. Kaufman, Y. Rudich, Y., and J. V. Martins (2007), On the twilight
530 zone between clouds and aerosols, *Geophys. Res. Lett.*, 34, L08805,
531 doi:10.1029/2007GL029253.
532 Levy, R.C., L.A. Remer, R.G. Kleidman, S. Mattoo, C. Ichoku, R. Kahn, and T.F. Eck (2010),
533 Global evaluation of the Collection5 MODIS dark-target aerosol products over land, *Atmos*.
534 *Chem*. *Phys*., 2010;10:10399–420.
535 Loeb, N. G., and G. L. Schuster (2008), An observational study of the relationship between
536 cloud, aerosol and meteorology in broken low-level cloud conditions, *J. Geophys. Res.*, 113,
537 D14214, doi:10.1029/2007JD009763.
538 Lyapustin, A. and Y. Kaufman (2001), The role of adjacency effect in the optical remote sensing
539 of aerosol *J Geophys Res*, *106*: 11909-11916.
540 Marshak, A., A. Davis, W. Wiscombe, and R.F. Cahalan (1995), Radiative smoothing in fractal
541 clouds *J. Geophys. Res. (Atmos.)*, *100*, 26247-26261
542 Marshak, A., G. Wen, J. Coakley, L. Remer, N.G. Loeb, and R.F. Cahalan (2008), A simple
543 model for the cloud adjacency effect and the apparent bluing of aerosols near clouds *J.*
544 *Geophys. Res.*, *113*(D14S17) doi:10.1029/2007JD009196.
545 Marshak, A., K.F. Evans, T. Várnai, and G. Wen (2014), Extending 3D near-cloud corrections
546 from shorter to longer wavelengths *J. Quant. Spec. Rad. Trans*, *147*, 79-85,
547 doi:10.1016/j.jqsrt.2014.05.022.

548 Martins, J. V., D. Tanré, L. Remer, Y. Kaufman, S. Mattoo, and R. Levy (2002), MODIS Cloud
549 screening for remote sensing of aerosols over oceans using spatial variability, *Geophys. Res.*
550 *Lett.*, 29(12), doi:10.1029/2001GL013252.
551 Odell, A. P. and J. A. Weinman, (1979), The effects of atmospheric haze on images of the
552 Earth's surface, *J. Geophys. Res.*, 80(36),5035-5040, doi:10.1029/JC080i036p05035.
553 Otterman, J. and R. S. Fraser (1979), Adjacency effects on imaging by surface reflection and
554 atmospheric scattering: cross radiance to zenith, *Appl. Opt.*, 18, 2852-2860, doi:
555 10.1364/AO.18.002852.
556 Pincus, R. and B. Stevens (2009), Monte Carlo spectral integration: A consistent approximation
557 for radiative transfer in large eddy simulations, *Journal of Advances in Modeling Earth*
558 *System*, June 2009, doi:10.3894/JAMES.2009.1.1.
559 Platnick, S., M. King, S. Ackerman, et al. (2003), The MODIS cloud products: Algorithms and
560 examples from Terra, *IEEE Trans Geosci Remote Sens*, **41 (2):** 459-473.
561 Redemann, J., Q. Zhang, P. B. Russell, J. M. Livingston, and L. A. Remer (2009), Case Studies
562 of Aerosol Remote Sensing in the Vicinity of Clouds, *J. Geophys. Res.*, 114, D06209,
563 doi:10.1029/2008JD010774.
564 Remer, L.A., Y.J. Kaufman, D. Tanre, S. Mattoo, D.A. Chu, J.V. Martin, R.-R. Li, C. Ichoku,
565 R.C. Levy, R.G. Kleidman, T.F. Eck, E. Vermote, and B.N. Bolben (2005), The MODIS
566 Aerosol Algorithm, Products, and Validation, *J. Geophy. Res.*, Vol 62, 947-973.
567 Rienecker, M.M., M.J Suarez, R. Gelaro, R. Todling, J. Bacmeister, E. Liu, et al. (2011),
568 MERRA:NASAs modern-era retrospective analysis for research and applications, *J. Clim.*,
569 24:3624–48.

570 Su, W., G. L. Schuster, N. G. Loeb, R. R. Rogers, R. A. Ferrare, C. A. Hostetler, J. W. Hair, and
571 M. D. Obland (2008), Aerosol and cloud interaction observed from high spectral resolution
572 lidar data, *J. Geophys. Res.*, 113, D24202,doi:10.1029/2008JD010588.
573 Stevens, B., C.-H. Moeng, P. P. Sullivan (1999), Large-Eddy Simulations of radiatively driven
574 convection: sensitivities to the representation of small scales, *J. Atmos. Sci.*, 56:3963-84.
575 Tackett, J. L. and L. Di Girolamo (2009), Enhanced aerosol backscatter adjacent to tropical trade
576 wind clouds revealed by satellite-based lidar, *Geophys. Res. Lett.*, 36, L14804,
577 doi:10.1029/2009GL039264.
578 Twohy, C. H., J. A. Coakley Jr., and W. R. Tahnk (2009), Effect of changes in relative humidity
579 on aerosol scattering near clouds, *J. Geophys. Res.*, 114, D05205,
580 doi:10.1029/2008JD010991.
581 Titov, G. A. (1990), Statistical description of radiation transfer in clouds, *J. Atmos. Sci.*, 47, 24 –
582 38, doi:10.1175/1520-0469(1990)047<0024:SDORTI>2.0.CO;2.
583 Várnai, T. and A. Marshak (2011), Global CALIPSO observations of aerosol changes near
584 clouds, *Geosci. Remote Sens. Lett. 19-23*, *8, Issue 1*, 19-23
585 doi:10.1109/LGRS.2010.2049982.
586 Varnai, T. and A. Marshak (2012) Analysis of co-located MODIS and CALIPSO observations
587 near clouds *Atmos Meas Tech*, *5*(2): 389-396, doi:10.5194/amt-5-389-2012.
588 Varnai, T. and A. Marshak (2014), Near-cloud aerosol properties from the 1 km resolution
589 MODIS ocean product *J. Geophys. Res. Atmos.*, *119*(3): 1546-1554
590 doi:10.1002/2013JD02063.

591 Vermote, E.F., D. Tanre, J. L. Deuze, M. Herman, and J.-J. Morcrette (1997), Second simulation
592 of the satellite signal in the solar spectrum, 6S: an overview, *IEEE Trans. Geosci. Remote*
593 *Sens.* 35, 675–686.
594 Wen, G., A. Marshak, R. F. Cahalan, L. A. Remer, and R. G. Kleidman (2007), 3-D aerosol-
595 cloud radiative interaction observed in collocated MODIS and ASTER images of cumulus
596 cloud fields, *J. Geophys. Res.*, 112, D13204, doi:10.1029/2006JD008267.
597 Wen, G., A. Marshak, and R.F. Cahalan (2008), Importance of Molecular Rayleigh Scattering in
598 the Enhancement of Clear Sky Radiance in the Vicinity of Boundary Layer Cumulus Clouds,
599 *J. Geophys. Res.*, 133(D24207)doi:10.1029/2008JD010592.
600 Wen, G., A. Marshak, R. C. Levy, L. A. Remer, N. G. Loeb, T. Várnai, and R. F. Cahalan
601 (2013), Improvement of MODIS aerosol retrievals near clouds, *J. Geophys. Res. Atmos*., 118,
602 9168–9181, doi:10.1002/jgrd.50617.
603 Yang, Y., and L. Di Girolamo (2008), Impacts of 3-D radiative effects on satellite cloud
604 detection and their consequences on cloud fraction and aerosol optical depth retrievals, *J.*
605 *Geophys. Res.*, 113, D04213, doi:10.1029/2007JD009095.
606 Yang, W., Marshak, A., Varnai, T., Wood, R. 2014. CALIPSO observations of near-cloud
607 aerosol properties as a function of cloud fraction, *Geophys. Res. Lett*, *41*: 9150-9157,
608 doi:10.1002/2014GL061896.
609 Zhuravleva, T., and A. Marshak (2005), On the validation of the Poisson model of broken
610 clouds, *Izv. Atmos. Oceanic Phys.*, 41(6), 713– 725.
611

612 **Figures**

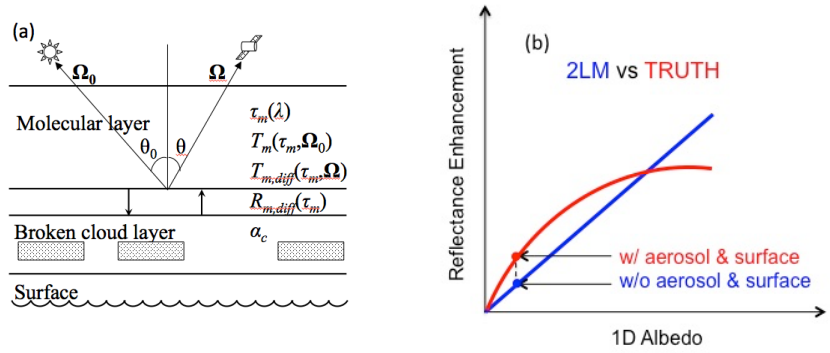

613

614 Fig. 1. (a) A sketch of the 2LM showing directions of the Sun ($\mathbf{\Omega_0}$) and satellite ($\mathbf{\Omega}$), solar zenith
615 angle (θ_0) and satellite viewing zenith angle (θ), properties of the molecular layer (i.e., τ_m:
616 molecular scattering optical depth, T_m: transmittance of solar radiation from above, $T_{m,diff}$:
617 transmittance of diffuse radiation from below, $R_{m,diff}$: reflectance of diffuse radiation from
618 below) for MODIS aerosol wavelength λ, and cloud albedo (α_c) (*Marshak et al.*, 2008). (b) A
619 sketch of the characteristics of 2LM estimated reflectance enhancement versus the truth.

620

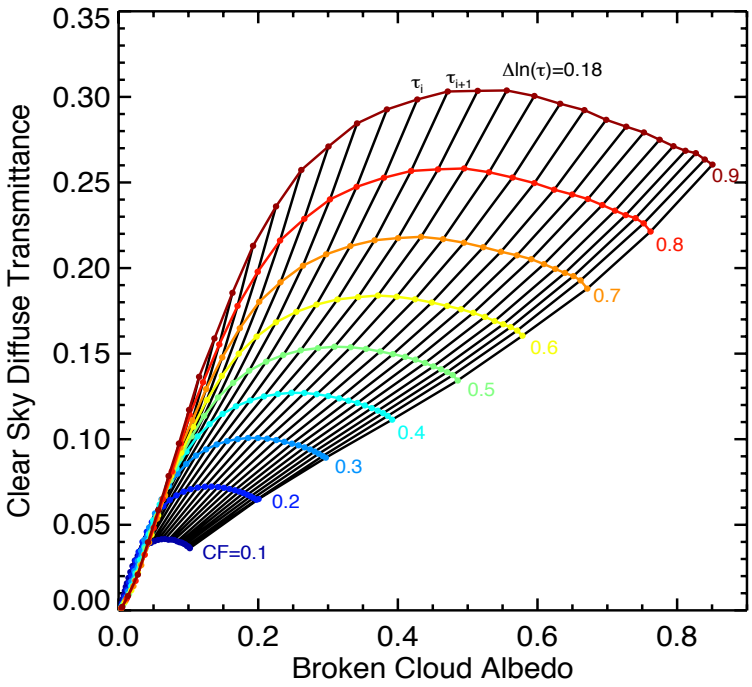

621

622 Fig. 2. Clear sky diffuse transmittance as a function of cloud albedo for different cloud fractions
623 (color lines) and average cloud optical depths (black lines). Cloud aspect ratio (*D/H*) is 2 and
624 SZA=36°. The cloud fraction ranges from 0.1 to 0.9 with increments of 0.1. The cloud optical
625 depth ranges from 0.1 to 158, where $\Delta\tau = 0.25$ for $\tau \leq 2$, and $\Delta\ln(\tau)=0.18$ for $\tau > 2$. Here $\tau_i =$
626 10.3, $\tau_{i+1} = 12.36$.

627

628

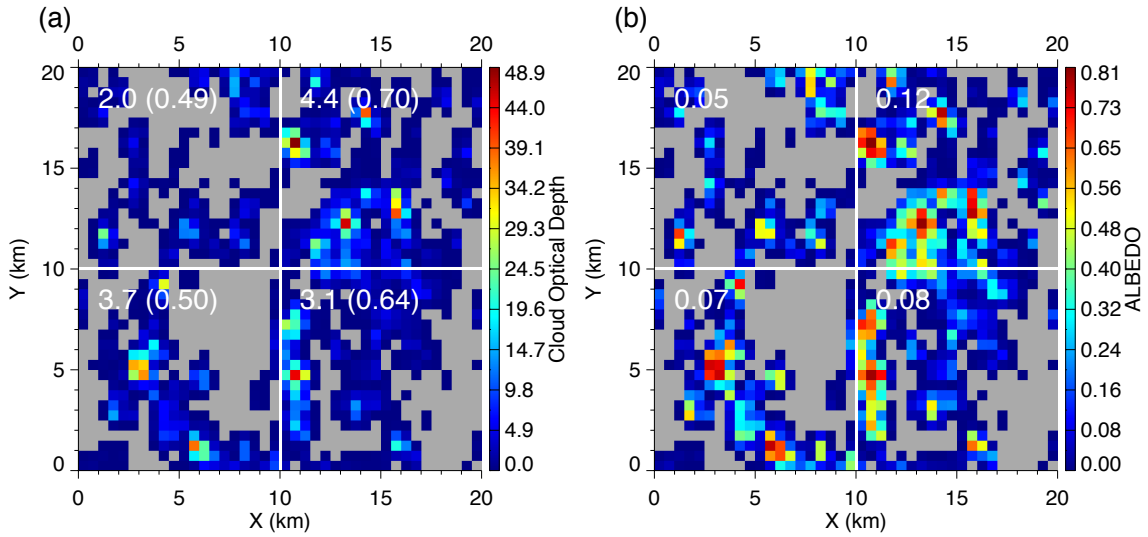

Fig. 3. (a): An example of the LES-simulated 20 km x 20 km cloud optical depth field with grey color for clear (mean optical depth of cloudy pixels is 3.4 and cloud fraction is 0.58). Average optical depth for cloudy pixels and cloud fraction (in parenthesis) are indicated for each 10 km x 10 km box. (b): 1D cloud albedo for the cloud field in the left panel with SZA = 26.1°. Albedo of clear pixels in grey is zero. Domain average albedo over cloudy and clear pixels is 0.079. The average albedo for each 10 km x 10 km box is indicated.

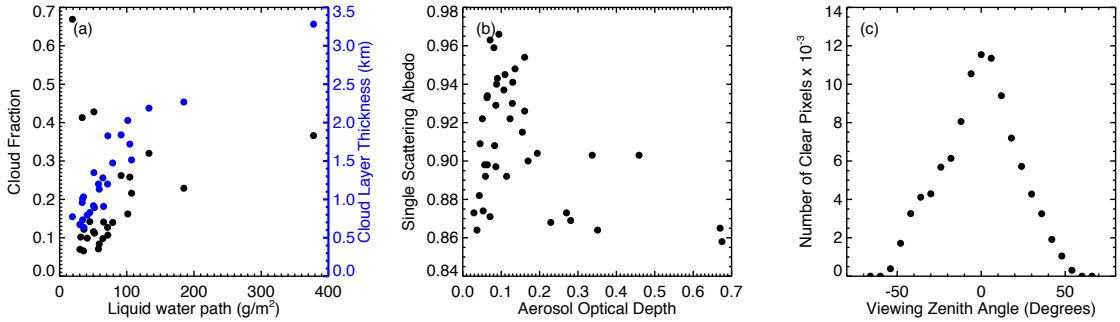

638
639 Fig. 4. Cloud and aerosol properties of LES simulated cumulus cloud fields. (a) cloud fraction
640 and cloud layer thickness as a function of liquid water path, (b) aerosol single scattering albedo
641 as a function of aerosol optical depth, (c) clear pixels identified by the MOD04 mask as a
642 function of viewing zenith angle.

643

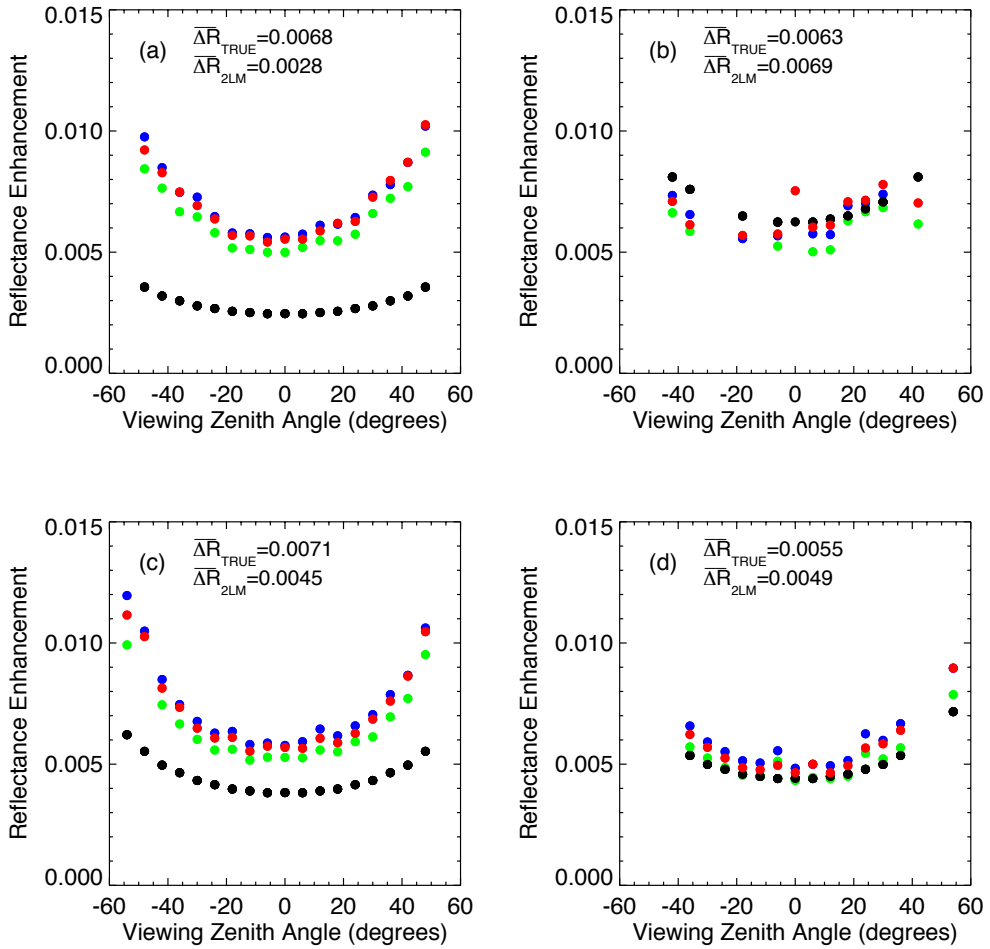

644

645
646

647 Fig. 5. Reflectance enhancement as a function of viewing zenith angle for the 2LM estimates
648 (black dots) and the truth (color dots) for the four 10 km x 10 km sub-images in Fig. 4a. For the
649 truth, three aerosol profiles with AOD of 0.045, 0.083, 0.194 are indicated by green, blue, and
650 red, respectively. The average of all reflectance enhancements of 2LM is 0.0045 compared to the
651 truth of 0.0065.

652

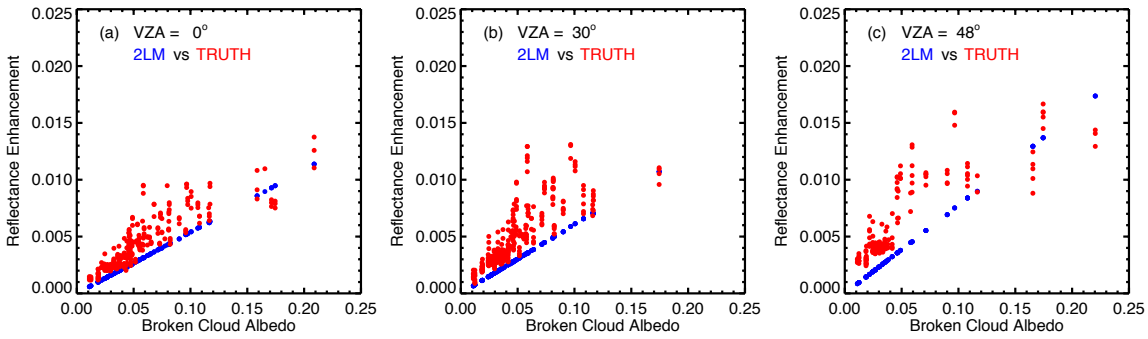

653
654 Fig. 6. Compare 2LM reflectance enhancements (blue) with the truth (red) for (a) nadir, (b)
655 oblique view-angles for all cloud scenes.

656

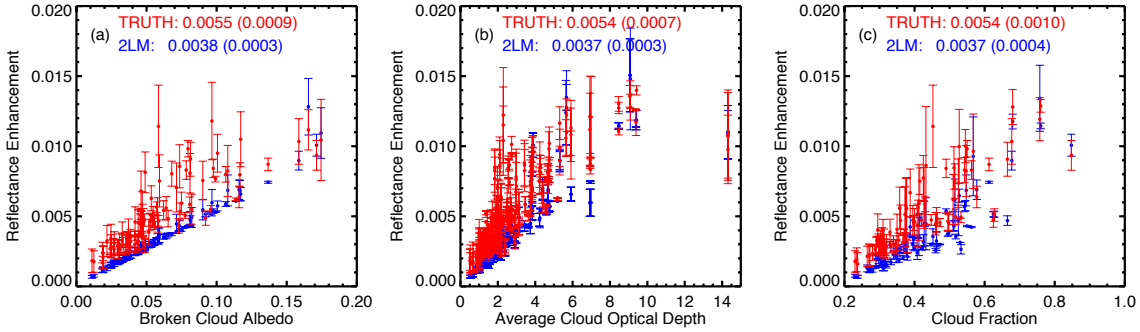

Fig. 7. 2LM estimated reflectance enhancement (red) and the truth (blue) as a function of (a) cloud albedo, (b) cloud optical depth, and (c) cloud fractions. The mean values of average enhancement and standard deviation (in parentheses) are indicated.

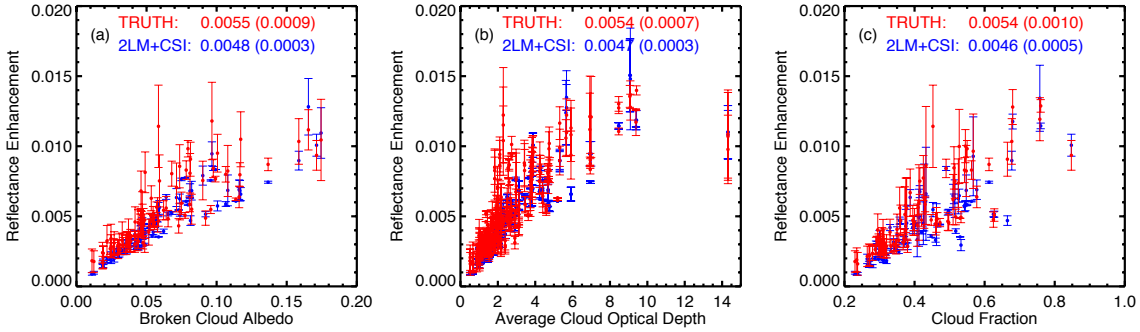

663
664 Fig. 8. Similar to Fig. 7 but the red for 2LM+CSI estimated reflectance enhancements.

665

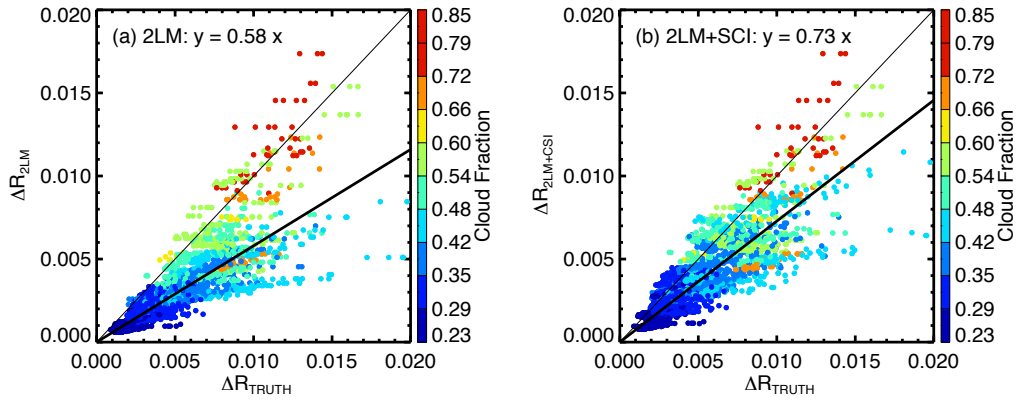

666

667 Fig. 9. Compare (a) 2LM and (b) 2LM+CSI estimated reflectance enhancements with the truth
668 with cloud fraction indicated by colors. Increase of the slope as model includes more physical
669 mechanism is evident.

670

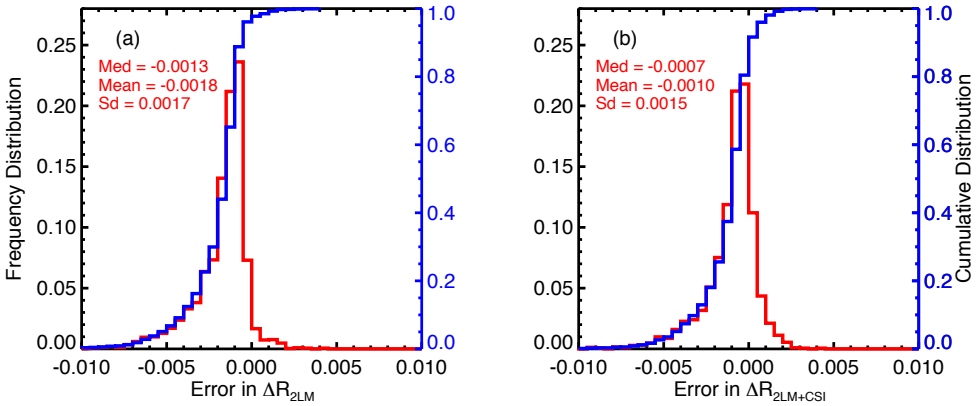

671

672 Fig. 10. Distributions of errors in modeled reflectance enhancement (a) for 2LM and (b) for
673 2LM+CSI with median (Med), mean (Mean), and standard deviation (Sd) indicated. For the true
674 mean reflectance enhancement (Fig. 11), mean errors are -36% and -20% for 2LM and
675 2LM+CSI, respectively.

676

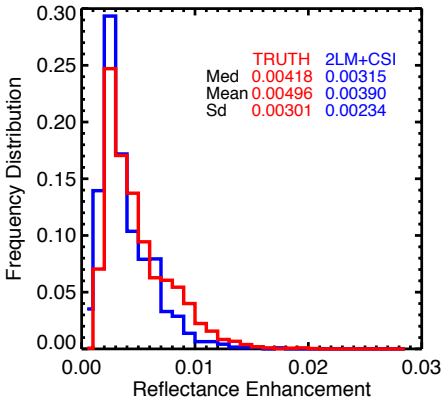

677

678 Fig. 11. Distributions of 2LM+CSI (blue) and the true (red) reflectance enhancement with
679 median (Med), mean (Mean), and standard deviation (Sd) indicated.

680

681

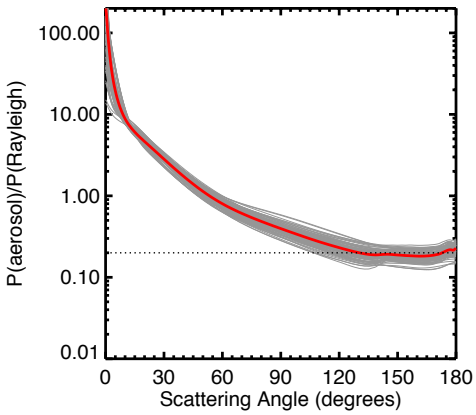

682

683 Fig. 12. The ration of aerosol scattering phase function to Rayleigh scattering phase function for
684 the 40 different aerosols (grey) in LES/SHDOM simulations and average value (red).

685

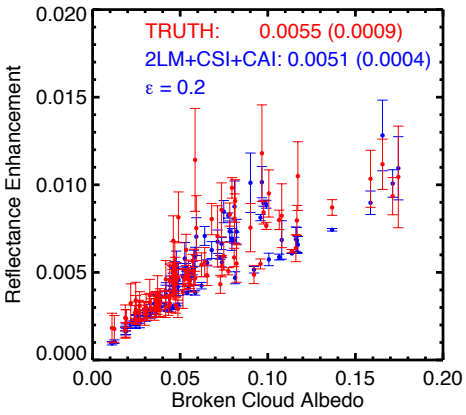

686

687 Fig. 13. Similar to Fig. 8a but with additional cloud-aerosol interactions assuming ε = 0.2.